Joachimski et al.: Five million years of high atmospheric CO_2 in the aftermath of the Permian-Triassic mass extinction

SAMPLE LOCATIONS

Late Permian and Early to Middle Triassic pedogenic carbonate samples derive from sections in Russia (Southern Ural foreland basin), China (Shanxi, Shaanxi, Henan and Xinjiang provinces), South Africa (Karoo Basin) and the UK (Devon). Early Triassic pedogenic carbonates from Russia derive from the Southern Ural foreland basin (Orenburg area) which during Late Permian to Early Triassic times was at paleolatitudes of 30–35° N (Van der Voo and Torsvik, 2004; Newell et al., 1999). Late Permian overbank deposits with channeled sandstone deposits are overlain by coarse fluvial conglomerates and sandstones of Early Triassic age (Newell et al., 1999). The continental succession was dated primarily using biostratigraphy (ostracods and vertebrates) and magnetostratigraphy (Newell et al., 1999; Tverdokhlebov et al., 2005). The Late Permian and Early Triassic paleosols were studied in detail by Kearsey et al. (2012) with both calcitic and dolomitic pedogenic nodules occurring. Dolomitic paleosols are most abundant in the late Changhsingian, while Early Triassic paleosols contain no dolomite. The micro- to cryptocrystalline matrix of dolomitic nodules is composed of dolomitic rhombs of 2 to 5 μm size and shows a clotted texture, commonly associated with formation in vadose environments. The observation that secondary diagenetic carbonate in veins and open space structures is exclusively represented by calcite and never by dolomite as well as that dolomitic nodules only occur in latest Permian but not in the Early Triassic sediments has been taken as evidence that dolomite was precipitated as a primary mineral phase during pedogenesis (see Kearsey et al. (2012) for further details). Further, pCO_2 estimates from paleosols from China and South Africa agree relatively well with pCO_2

estimates derived from the dolomitic pedogenic nodules from the Ural foredeep giving us confidence that the dolomitic nodules represent primary precipitates.

The Taodonggou section (NW China, Xinjiang Province) is located in the southern foothills of the Bogda Mountains in the northwestern part of the Turpan-Jungar Basin which during the Late Permian to Early Triassic was located at around 45° N. The sedimentary environment is interpreted as fluvial and deltaic in the Late Permian and as mudflat (lake plain) and floodplain with fluvial channels in the Early Triassic (Thomas et al. 2011, Yang et al., 2010*)*. The Permian-Triassic transition has been placed biostratigraphically (Liao et al., 1987; Liu, 2000) within a 30 m thick interval at the transition of the Guodikeng (Changhsingian) to Juicaiyuan Formation (Induan). The Late Permian and Early Triassic in North China (Henan, Shaanxi and Shanxi provinces) is represented by bioturbated fine-grained sandstones, reddish siltstones and mudstones containing Paleozoic-type plants (Sunjiagou Fm., Changhsingian) followed by mainly non-bioturbated reddish to brown-reddish fine-grained sandstones (Liujiagou Fm., Early Triassic) with the Early Triassic plant *Pleuromeia* occurring the upper part of the formation (Chu et al., 2017).

The sedimentary sequence in the Karoo Basin has been studied intensively for sedimentary facies and tetrapod populations (Keyser and Smith, 1978; Rubidge et al., 1995). Based on abundant tetrapod faunas, the Permian-Triassic boundary has traditionally been placed at the transition of the *Daptocephalus* tetrapod assemblage Zone (AZ; Late Permian) to the *Lystrosaurus* AZ (Early Triassic). The *Daptocephalus* AZ fauna occurs in greyish siltstones with intercalated ribbon sandstones and thin sand sheets of the Late Permian Balfour Fm. These sediments were deposited in a meandering fluvial setting. A change to red-coloured siltstones with an increasing frequency and thickness of intercalated sandstones characterizes the Palingkoff Mb. (Uppermost Beaufort Fm.; latest Permian to earliest Triassic). Sediments of the Palingkoff Mb. were interpreted to have been deposited in wide ephemeral streams (Smith,

1995) forming the precursors of the braidplains that characterize the depositional setting of the overlying Early Triassic sediments of the Katberg Fm. Sample NWP1 was taken from the New Wapadsberg pass section from approximately 70 m below the assumed PTB (see Gastaldo et al. (2014) for detailed description). Sample OLP4 is from the Old Lootsberg pass section and represents a carbonate nodule from a pedogenic nodule conglomerate (lag deposit) from the lower Katberg Fm. (Early Triassic; see Neveling et al. (2016) for detailed description).

The Otter Sandstone Fm. exposed at the south Devon coast (Great Britain) is of lower to middle Anisian age (Hounslow and McIntosh, 2003) and is represented by aeolian and stacked fluvial channel sandstones with locally reworked calcretes in channel lags as well vertical rhizoconcretions (Purvis and Wright, 1991). Samples were collected from the coastal exposures east of Budleigh Salterton (East Devon).

Relative ages of the samples were estimated based on the position of the samples in the measured sections and the available magnetostratigraphic and biostratigraphic information by assuming constant sedimentation rate for the dated time intervals.

CLASSIFICATION OF PEDOGENIC NODULES

A total of 105 pedogenic carbonate samples were collected from the various sections (Table S1). Most carbonate nodules were collected from 40 to 150 cm below overlying fluvial silt- to sandstone beds generally cutting into the floodplain deposits. We rarely observed larger-scale paleosol structures (e.g. slickensides) or distinct erosive boundaries within the 50 cm of overlying sediment. Given compaction as well as erosional removal of the topmost parts of the soil profiles, we assume that carbonate nodules formed at > 50 cm depth in the soils.

Figure S1: Calcisols (Stage II) from NW China and Russia showing rare to abundant pedogenic nodules (stage II). A - Taondonggou W Section (Xinjiang Province, Northwest China; sample TD5) showing rhizoconcretions and carbonate nodules ; B - Taondonggou W Section (Xinjiang Province, Northwest China; sample TD14); C - Boyevaya Gora section (Southern Ural foredeep, Russia; sample DYL-Z); D - Liulin Section (Shanxi Province, North China; sample LL 6); E - Boyevaya Gora Section (Southern Ural foreland basin, Russia; sample BG 5); F - Dayulin section (Henan Province, North China; sample BG12). Size of sample bags is 12 x 8 cm

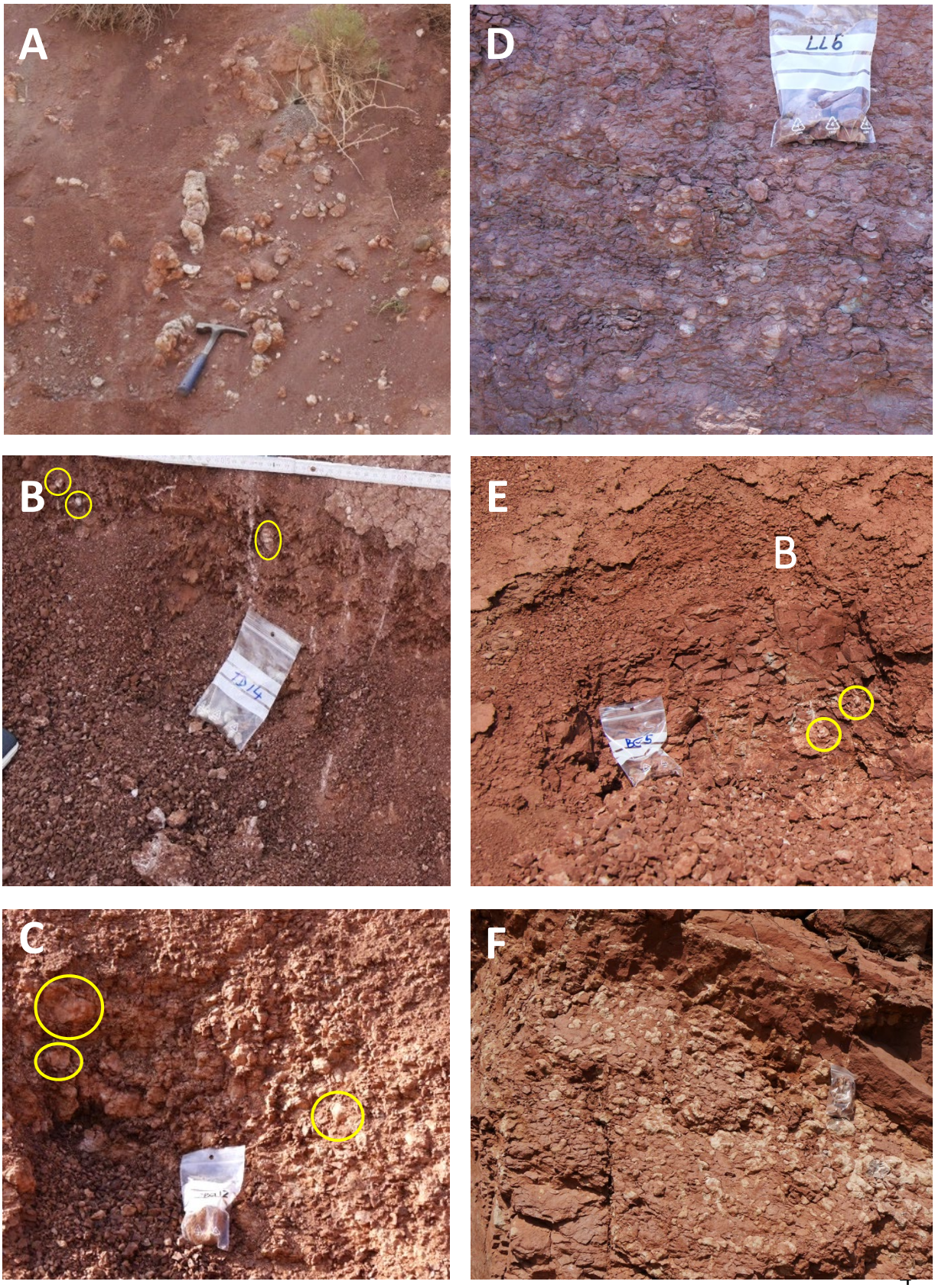

All studied paleosols were classified as calcisols (Mack et al., 1993; except pedogenic nodule conglomerate from Old Lootsberg Pass/Karoo which represents a fluvial lag deposit) and are characterized by rare to common carbonate nodules (up to several cm in size; Stage II; Figure S1) or more rarely by stacked nodules and rhizocretions (Stage II). Thin sections of all samples were studied for pedogenic features in order to characterize the environment of formation (e.g. non-saturated vs. saturated soil zone; Figure S2). Based on thin section features and carbon isotope ratios ($\delta^{13}C_{hypo,}$ see below), 46 pedogenic carbonate samples were accepted as having formed in the non-saturated soil zone and used for atmospheric CO_2 reconstruction (Table S4). The matrix of the nodules is characterized by a crystic plasmic fabric (Brewer 1964) with patches of crystal sizes ranging from micrite to microspar with a clear dominance of micrite. Most nodules exhibit alpha-fabric (abiogenic) features as floating, etched or exploded grains, circum-granular cracking and globular structures. Beta-fabric (biogenic, mainly fungal and root related) features as rhizoliths were present as root molds and root tubules preserved as roundish voids of 0.1 to 1 mm diameter cemented by sparite. The rhizoliths either consist of relatively homogenous micrite distinctly separated from the carbonate matrix by color or grain size or show a more complex structure of concentric laminae or a cellular structure. In part, rhizoliths are encompassed by circum-granular cracks resulting from displacive carbonate growth. Alveolar septal structures (Wright 1986) were frequently observed in nodules comprising rhizoliths.

Figure S2: Thin section photomicrographs showing typical pedogenic features of abiogenic alpha and biogenic beta fabrics. TD16: well-developed floating grain (fg) fabric and circumgranular cracking (cgc), both related to displacive carbonate precipitation in soils. Structures attributed to root growth include rhizocretions (rhi) as well as irregular and roundish root molds or casts filled by sparite. TD17: fg fabric, rhizocretion and cgc. Irregular voids filled by sparite resembling root casts or molds. BG4: fg fabric and abundant and distinct glaebules (gl) or peloids surrounded by cgc. Aggregated coated grain (acg) in the lower left. DYL-X: Glaebular fabric with cgc and matrix brecciation as a result of displacive carbonate precipitation. TD 13: Rhizocretion with concentric micritic to microsparitic laminae surrounded by cgc. SMB 4b: Carbonate nodule showing pronounced fg fabric and features as cgc and gl. TD - Taodonggou section (Xinjiang/China), DYL – Dayulin B section (Henan/North China), BG - Boyevaya Gora section (South Urals/Russia), SMB – Sambullak section (South Urals/Russia).

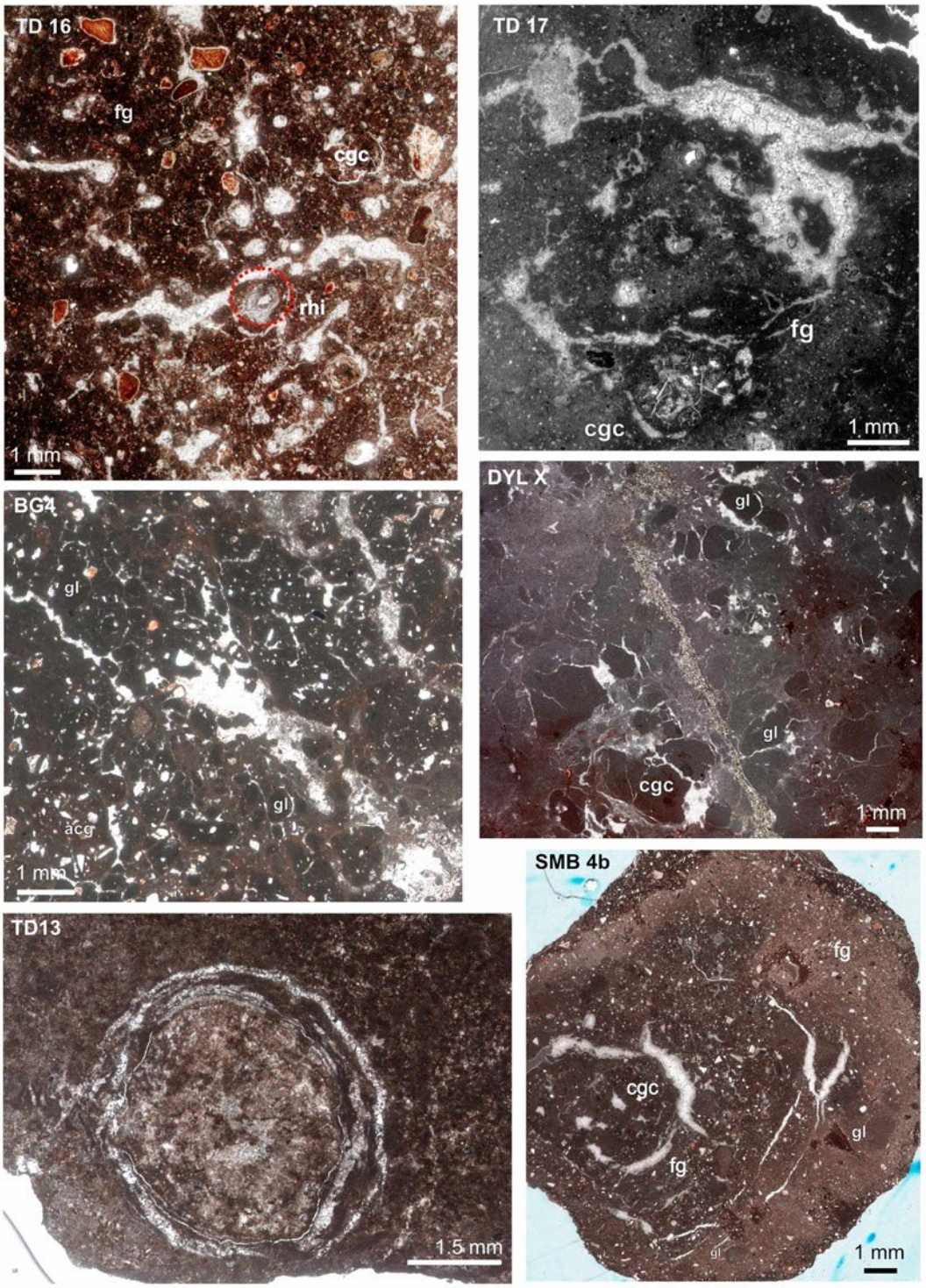

Formation in the non-saturated zone was further evaluated by comparing the carbon isotope ratios of soil carbonate and soil organic matter. For soil carbonates precipitated under well-aerated or non-saturated conditions, total soil CO_2 is derived from microbial oxidation of soil organic matter (SOM), root respiration as well as atmospheric CO_2. Instead in waterlogged soils, atmospheric CO_2 will not contribute to total soil CO_2 (Cerling, 1984; Tabor et al. 2007). Pedogenic carbonate formed under closed system conditions will be around 14.8‰ (exact value depends on soil temperature) heavier than oxidizing organic matter, while carbonates formed in open system conditions will have higher $\delta^{13}C$ values due to the admixture of atmospheric CO_2 enriched in ^{13}C.

In order to further evaluate whether studied pedogenic carbonates were precipitated under open system conditions, the carbon isotope composition of a hypothetical carbonate ($\delta^{13}C_{hypo}$) precipitated from soil-CO_2 derived exclusively from the oxidation of SOM was calculated by applying a +4.4‰ correction to account for the more rapid diffusion of $^{12}CO_2$ relative to $^{13}CO_2$ through the soil matrix (Cerling, 1984) and the temperature dependent carbon isotope fractionation between soil CO_2 and carbonate (Romanek et al., 1992). $\delta^{13}C_{hypo}$ is in all cases lower than $\delta^{13}C$ of studied pedogenic calcites and dolomites which further supports the interpretation that the carbonates formed in open system conditions under the influence of atmospheric CO_2 (Table S4).

MATERIAL AND METHODS

Stable isotope analyses: Micritic areas were microsampled for carbonate carbon isotope analysis from polished rock slabs using a hand-held microdrill as micrite is considered as the most appropriate texture to ensure that pedogenic calcite preserves records of open system exchange with atmospheric CO_2 (Cerling, 1984; Tabor et al., 2007). Carbonate powders were reacted with 100% phosphoric acid at 70°C using a Gasbench II connected to a ThermoFisher

Delta V Plus mass spectrometer. All values are reported in per mil relative to V-PDB ((Vienna-PDB). Reproducibility and accuracy were monitored by replicate analysis of laboratory standards calibrated by assigning $\delta^{13}C$ values of +1.95‰ to NBS19 and -46.6‰ to LSVEC and $\delta^{18}O$ values of -2.20‰ to NBS19 and -23.2‰ to NBS18. Reproducibility for $\delta^{13}C$ was ±0.06‰ (1σ).

$\delta^{13}C$ of organic carbon was measured on sedimentary organic carbon (SOM) occluded in the in the pedogenic nodules. Powdered pedogenic carbonates were dissolved in 10% HCl. Insoluble residues were neutralized by washing repeatedly with de-ionized water, dried at 60°C and following homogenized and weighed for isotope analysis. Carbon isotope analyses of SOM was performed with a Flash EA 2000 elemental analyzer connected online to ThermoFisher Delta V Plus mass spectrometer. All carbon isotope values are reported in the conventional δ-notation in permil relative to V-PDB. Accuracy and reproducibility of the analyses were determined by replicate analyses of laboratory standards calibrated to international standards USGS 40 and 41. Reproducibility was ±0.05‰ (1σ). The carbon isotope values of organic carbon were not corrected by -1‰ for a potential enrichment in ^{13}C during organic carbon decomposition (e.g. Myers et al. 2016).

Paleosol pCO_2 barometer

Atmospheric CO_2 concentrations were calculated from the carbon isotopic composition of soil carbonate precipitated in the well-drained soils by applying the two-component carbon isotope mixing model given that soil CO_2 is a mixture of two isotopically different CO_2 sources, soil respired CO_2 and atmospheric CO_2 (Cerling, 1984; 1991).

$$[CO_2]_{atm} = S(z) \cdot \frac{(\delta^{13}C_s - 1.0044 \cdot \delta^{13}C_{resp} - 4.4)}{\delta^{13}C_{atm} - \delta^{13}C_s} \quad (1)$$

S(z) is the soil respired CO_2 concentration, $\delta^{13}C_s$, $\delta^{13}C_{resp}$ and $\delta^{13}C_{atm}$ represent the carbon isotopic composition of total soil CO_2, soil respired CO_2 and atmospheric CO_2, respectively.

$\delta^{13}C_s$, $\delta^{13}C_{resp}$ and $\delta^{13}C_{atm}$ are calculated from the measured carbon isotope composition of pedogenic carbonate, soil organic matter (SOM) and marine carbonate, respectively.

We estimated S(z) following Montanez (2013) who compiled a large stable isotope dataset for Holocene soils to determine S(z) for different soil orders. The difference in $\delta^{13}C$ of modern soil carbonate and SOM ($\Delta_{carb\text{-}org}$) was used to further constrain S(z). For modern protosols and calcisols having $\Delta_{carb\text{-}org}$ of 12.2 to 15.8‰, a S(z) range of 500 to 2500 ppmV with a best S(z) estimate between 1500 and 2000 ppmv is observed (Montanez 2013). However, all studied Permian and Early Triassic calcisols show $\Delta_{carb\text{-}org}$ values > 15.8‰ (Table S4) suggesting that carbonate precipitation occurred during periods of low soil productivity and that atmospheric CO_2 was probably a large component of soil CO_2. In our study, $\Delta_{carb\text{-}org}$ is in all cases > 16‰ and for 75% of all samples > 18‰. According to Montanez (2013), $\Delta_{carb\text{-}org}$ > 16‰ is indicative of soil atmospheres ≤2000 ppmv, while for $\Delta_{carb\text{-}org}$ > 18‰ or higher, soil respired CO_2 is likely ≤1000 ppmv. Following, we argue that carbonate nodules originated from low-productivity drylands with S(z) between 500 to 1500 ppmV.

$\delta^{13}C_{resp}$ equals $\delta^{13}C$ of organic matter of the pedogenic nodules. $\delta^{13}C_a$ (Table S3) is calculated from $\delta^{13}C$ of marine carbonates utilizing the $CO_{2(g)}$ - calcite fractionation factor of Romanek et al. (1992). As the carbon isotope fractionation between carbon dioxide and calcite is dependent on temperature, water temperature during precipitation of the marine carbonates has to be assessed. We use the carbon isotope record (Sun et al. 2012; Shen et al. 2013) as well oxygen isotope temperatures (Joachimski et al. 2012, Sun et al. 2012) published for South China as conodonts analyzed for oxygen isotopes derive from the same carbonates used to reconstruct the carbon isotope record. By this we make sure that reconstructed temperatures are close to water temperature during carbonate precipitation.

Soil temperature and S(z) in particular are the variables that most strongly influence the calculated atmospheric CO_2 concentrations, as shown in Figure S3.

Statistical data processing

We used the Tidyverse package (Wickham et al., 2019) for data processing. Quantile intervals have been calculated according to Kruschke, J. K. (2011). All scripts used to conduct analyses are available at https://github.com/Ischi94/Joachimski.

Figure S3: Effect of S(z) and soil temperature (T) on reconstructed atmospheric pCO_2 illustrated for samples BG5 (Changhsingian) and TD18 (Griesbachian): A-B) S(z) varying between 500 to 2000 ppmV, all other variables including soil temperature constant; C-D) Soil temperature varying by ± 5°C around reconstructed mean soil temperature, all other variables constant including S(z). Vertical dotted lines corresponds to measured $\delta^{13}C$ of pedogenic calcite, horizontal dotted lines give calculated minimum and maximum atmospheric pCO_2. Note significant influence of S(z) on pCO_2

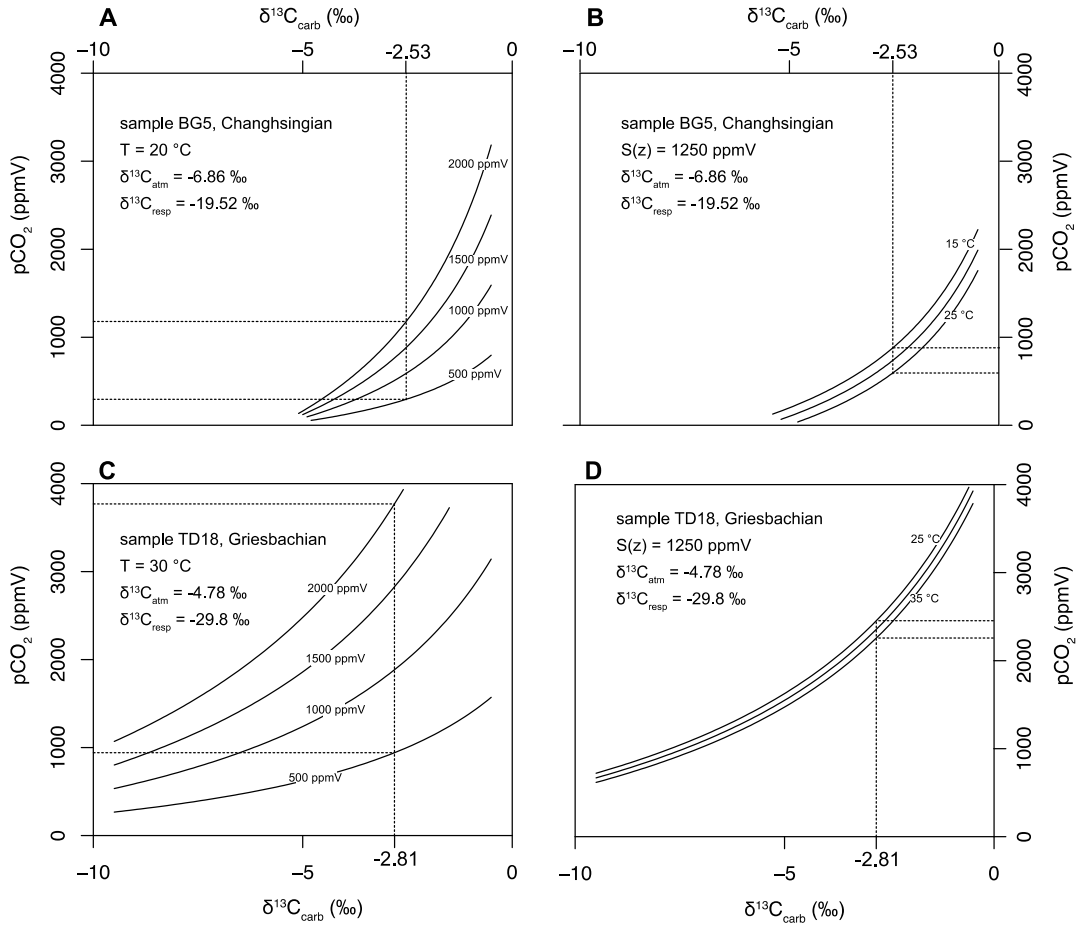

SUPPLEMENTAL REFERENCES

Brewer, R., 1964, Fabric and mineral analysis of soils: 470 pp. John Wiley & Sons, London and New York.

Cerling T. E., 1984, The stable isotopic composition of modern soil carbonate and its relationships to climate: Earth and Planetary Science Letters, v. 71, p. 229–240.

Cerling, T.E., 1991, Carbon dioxide in the atmosphere: evidence from Cenozoic and Mesozoic paleosols: American Journal of Science, v. 291, p. 377–400.

Chu, D., Tong, J., Bottjer, D.J., Song, H., Song, H., Benton, M.J., Tian, L., and Guo, W., 2017, Microbial mats in the terrestrial Lower Triassic of North China and implications for the Permian–Triassic mass extinction: Palaeogeography, Palaeoclimatology, Palaeoecology, v. 474, p. 214-231.

Gastaldo, R.A, Knight, C.L., Neveling, J., and Tabor, N.J., 2014, Latest Permian paleosols from Wapadsberg Pass, South Africa: Implications for Changhsingian climate: Geological Society of America Bulletin, v. 126, p. 665-679.

Hounslow, M.W. and McIntosh, G., 2003, Magnetostratigraphy of the Sherwood Sandstone Group (Lower and Middle Triassic), south Devon, UK: detailed correlation of the marine and non-marine Anisian: Palaeogeography, Palaeoclimatology, Palaeoecology, v. 193, 325-348.

Hu, Q. and Feng, S., 2013, A daily soil temperature dataset and soil temperature climatology of the contiguous United States: Journal of Applied Meterology, v. 42, p. 1139-1156.

Joachimski, M.M., Alekseev, A.S., Grigoryan, A., and Gatovsky, Yu.A., 2020, Siberian Trap volcanism, global warming and the Permian-Triassic mass extinction: new insights from Armenian Permian-Triassic sections: Geol. Soc. Am. Bull., v. 132, p. 427-443.

Kruschke, J. K., 2011, Doing Bayesian data analysis: a tutorial with R and BUGS: Burlington, MA, Academic Press/Elsevier Elsevier.

Kearsey, T., Twitchett, R.J., and Newell, A.J., 2012, The origin and significance of pedogenic dolomite from the Upper Permian of the South Urals of Russia: Geological Magazine, v. 149, p. 291-307.

Keyser, A.W. and Smith, R.H.M., 1978, Vertebrate biozonation of the Beaufort Group with special reference to the Western Karoo Basin: Annales Geological Survey, v. **12**, p. 1-35.

Liao, Z. et al., 1987, Carboniferous and Permian in the western part of East Mts. Tian Mountains: Guidebook Excursion 4. 11th International Congress of Carboniferous Stratigraphy and Geology, Beijing, China.

Liu, Z., 2000, The Permo-Triassic boundary at the northern margin of Tu–Ha Basin: Journal of Stratigraphy, v. 24, p. 310–314.

Mack, G.H., James, W.C., and Monger, H.C., 1993. Classification of paleosols: Geological Society of America Bulletin, v. 105, p. 129–136.

Montanez, I.P., 2013, Modern soil constraints on reconstructing deep-time atmospheric CO_2: Geochimica et Cosmochimica Acta, v. 101, p. 57-75

Myers, T.S., Tabor, N.J., Jacobs L.L., and Bussert, R., 2016, Effects of different organic-matter sources on estimates of atmospheric and soil pCO_2 using pedogenic carbonate: Journal of Sedimentary Research,v. 86, p. 800-812.

Neveling, J., Gastaldo, R.A., and Geissman, J.W., 2016, The Permo-Triassic boundary in the Karoo Basin: Field trip Guide Pre3, 35th International Geological Congress, p. 1-79.

Newell, A.J., Tverdokhlebov, V.P. and Benton, M.J., 1999, Interplay of tectonics and climate on a transverse fluvial system, Upper Permian, Southern Uralian Foreland Basin, Russia: Sedimentary Geology, v. 127, p. 11–29.

Ogg, J.G., Ogg, G.M., and Gradstein, F.M., 2016, Triassic, in Ogg, J.G., Ogg, G.M., and Gradstein, F.M., eds., The Concise Geologic Time Scale 2016, Elsevier, p. 133-149.

Parton, J.W., and Logan, J.E., 1981, A model for diurnal variation in soil and air temperature: Agricultural Meterology, v. 23, p. 205-216.

Purvis, K. and Wright, P., 1991, Calcretes related to phreatophytic vegetation from the Middle Triassic Otter Sandstone of South West England: Sedimentology, v. 38, p. 539-551.

Romanek, C.S., Grossman, E.L., and Morse, J.W., 1992, Carbon isotopic fractionation in synthetic aragonite and calcite: effects of temperature and precipitation rate: Geochimica Cosmochimica Acta, v. 56, p. 419–430.

Rubidge, B.S., Johnson, M.R., Kitchinh, J.W., Smith, R.M.H., Keyer, A.W., and Groenewald, G.H., 1995, An introduction to the biozonation of the Beaufort Group, in Rubidge, B.S., ed.,

Biostratigraphy of the Beaufort Group (Karoo Basin). South African Committee for Stratigraphy, Biostratigraphic Series, v. 1, p. 1-2.

Shen, S.-Z., Cao, C.Q., Zhang, H., Bowring, S.A., Henderson, C.M., Payne, J.L, Davydov, V.I., Chen, B., Yuan, D.X., Zang, Y.C., Wang, W., Zheng, Q.F., 2013, High-resolution $\delta^{13}C_{carb}$ chemostratigraphy from latest Guadalupian through earliest Triassic in South China and Iran. Earth and Planetary Science Letters, v. 375, p. 156-165.

Smith, R.M.H., 1995, Changing fluvial environments across the Permian-Triassic boundary in the Karoo Basin, South Africa and possible causes of tetrapod extinctions: Palaeogeography, Palaeoclimatology, Palaeoecology, v. 116, p. 81-104.

Sun, Y., Joachimski, M.M., Wignall, P.B., Yan, C., Chen, Y., Jiang, H., Wang, L., and Lai, X., 2012, Lethally hot temperatures during the early Triassic greenhouse: Science, v. 338, p. 366–370.

Tabor, N.J., Montanez, I.P., Steiner, M.B., and Schwindt, D., 2007. $\delta^{13}C$ values of carbonate nodules across the Permian-Triassic boundary in the Karoo Supergroup (South Africa) reflect a stinking sulfurous swamp, not atmospheric CO_2: Paleogeography, Paleoclimatology, Paleoecology, v. 252, p. 370-381.

Thomas, S.G., Tabor, N.J., Yang, W., Myers, T.S., Yang, Y., and Wang, D., 2011, Palaeosol stratigraphy across the Permian–Triassic boundary, Bogda Mountains, NW China: Implications for palaeoenvironmental transition through earth's largest mass extinction: Paleogeography, Paleoclimatology, Paleoecology, v.308, p. 41-64.

Tverdokhlebov, V.P., Tverdokhlebova, G.I., Minikh, A.V., Surkov, M.V., and Benton, M.J., 2005, Upper Permian vertebrates and their sedimentological context in the Southern Urals, Russia: Earth Science Reviews, v. 69, p. 27–77.

Upchurch, G.R., Kiehl, J., Shields, C., Scherer, J., and Scotese, C., 2015, Latitudinal temperature gradients and high-latitude temperatures during the latest Cretaceous: congruence of geologic data and climate models: Geology, v. 43, p. 683–686.

Van der Voo, R. and Torsvik, T.H., 2004, The quality of the European Permo-Triassic paleopoles and its impact on Pangea reconstructions: Geophysical Monographs, v. 145, p. 29–42.

Wickham, H., Averick, M., Bryan, J., Chang, W., D'Agostino McGowan L., Romain, F. et al., 2019, Welcome to the Tidyverse: Journal of Open Source Software, v. 4, 1686.

Wright, V.P., 1986, The role of fungal biomineralization in the formation of Early Carboniferous soil fabrics: Sedimentology, v. 33, p. 831–838.

Yang, W., Feng, Q., Liu, Y., Tabor, N., Miggins, D., Crowley, J.L., Lin, J., and Thomas, S., 2010, Depositional environments and cyclo- and chronostratigraphy of uppermost Carboniferous– Lower Triassic fluvial–lacustrine deposits, southern Bogda Mountains, NW China — A terrestrial paleoclimatic record of mid-latitude NE Pange: Global Planetary Change, v. 73, p. 15–113.

Zhang,L., Hay, W.W., Wang, C., and Gu, X., 2019, The evolution of latitudinal temperature gradients from the latest Cretaceous through the Present: Earth-Science Reviews, v. 189, 147-158.